

# Trawl-door Performance Analysis and Design Optimization with CFD

Eirikur Jonsson, Leifur Leifsson and Slawomir Koziel

*Engineering Optimization & Modeling Center, School of Science and Engineering, Reykjavik University, Reykjavik, Iceland*

**Keywords:** Trawl-doors, CFD, Design Optimization, Space Mapping, Surrogate-based Optimization, Variable-resolution Modeling, Simulation-driven Design.

**Abstract:** Rising fuel prices and inefficient fishing gear are hampering the fishing industry. In this paper, we present a computational fluid dynamic (CFD) model to analyse the hydrodynamic performance of trawl-doors, which are a major contributor to the high fuel consumption of fishing vessels. Furthermore, we couple the CFD model with an efficient design optimization technique and demonstrate how to redesign the trawl-door shapes for minimum drag at a given lift. The optimization technique is surrogate-based and employs a coarse discretization CFD model with relaxed convergence criteria. The surrogate model is constructed using the physics-based low-fidelity model and space mapping. The CFD model is applied to the analysis of current trawl-door shapes and reveals that they are operated at low efficiency (with lift-to-drag ratios lower than 1), mainly due to massively separated flow. An example design optimization case study reveals that the angle of attack can be reduced significantly by re-positioning and tilting the leading-edge slats. The performance can be improved by as much as 24 times (attaining lift-to-drag ratios around 24).

## 1 INTRODUCTION

Efficient trawler ships are vital for the fishing industry. Rising fuel prices have an enormous impact on the fishing industry as a whole as the cost of fuel is a major part of the operation cost. Most of the fuel (often over 80%) is spent during the trawling operation, which can take days at a time, although the trawling is normally performed at low speeds (less than 3 knots). The reason is the high drag of the fishing gear assembly. Therefore, a careful study and redesign of the assembly is necessary in order to reduce the fuel consumption and improve the efficiency.

A typical fishing gear assembly, shown in Fig. 1, consists of a large net, a pair of trawl-doors to keep the net open, and a cable assembly extending from the trawl-doors to the boat and the net. Although the trawl-doors are a small part of the fishing gear, they are responsible for roughly 30% of the total drag (Garner, 1967). A typical trawl-door is shown in Fig. 2.

Almost all the trawl-doors that have been developed over the years are fundamentally the same. Trawl-door designs are essentially steel plates, cut down, bent with a certain radius and welded together. These designs have two key elements, namely, the main element (ME), which is the largest part, and one

or more slats or slots, located at the leading edge. Minor design changes have been made to trawl-doors over the years, mainly because their designs are solely based on time consuming and expensive physical experiments.

Although, computational fluid dynamics (CFD) is widely used in design of a variety of engineering devices, such as aircraft, ships, and cars, very few applications are reported for trawl-doors in the literature (Haraldsson et al., 1996). Therefore, there is an opportunity to apply state-of-the-art CFD methods and optimization techniques to analyse and redesign the trawl-doors, before using physical experiments for verification purposes only. The trawl-doors have a low aspect ratio and are operated at high angles of attack (up to 50 degrees). As a result, the flow is highly three-dimensional and transient. A full three-dimensional simulation is required to capture the flow physics accurately. However, such simulation can be time consuming, and if used directly within the optimization loop (requiring a large number of simulations), the overall time of the design process becomes prohibitive. An efficient design methodology is therefore essential for such design applications.

In this paper, we develop a robust high-fidelity CFD method for the performance analysis of trawl-doors. As a first step in this development, we use

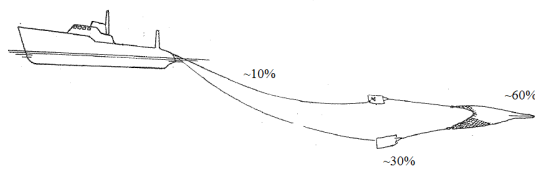


Figure 1: Trawl gear drag decomposition diagram (Garner, 1967). Approximately 30% of the drag of the entire fishing gear assembly is due to the trawl-doors. Cables account for about 10% and the net and other parts the rest.

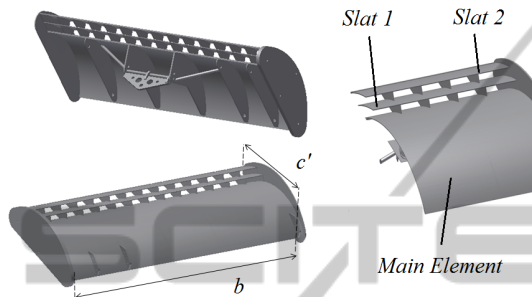


Figure 2: A CAD drawing of the F11 trawl-door elements. Main element (ME), Slat 1 and Slat 2. The span is  $b = 5.8m$  and the extended chord length is  $c' = 2.4m$ . This is a low aspect ratio wing with  $AR = 2.07$

a steady-state two-dimensional approach. The CFD model is used to investigate the performance of a typical trawl-door design. The CFD model is integrated within a recently developed surrogate-based optimization algorithm (Koziel and Leifsson, 2012) to demonstrate how trawl-doors can be redesigned for minimum drag at a given lift.

## 2 CFD MODELING

In this section, we describe the CFD model for two-dimensional trawl-door shapes. In particular, we describe the geometry, the computational grid, and the flow solver. We present results of a grid convergence study. Finally, we validate the model by comparing it's evaluations with experimental data.

### 2.1 Geometry

We consider a simple chord-wise cross-sectional cut of the F11 trawl-door (shown in Fig. 2). The two-dimensional cut is shown in Fig. 3. There are three elements, the main element (ME), which is the largest element of the assembly, slat 1, the middle element, and slat 2, the element farthest from the ME. The trawl-door is normalized with the chord length of the ME ( $c$ ).

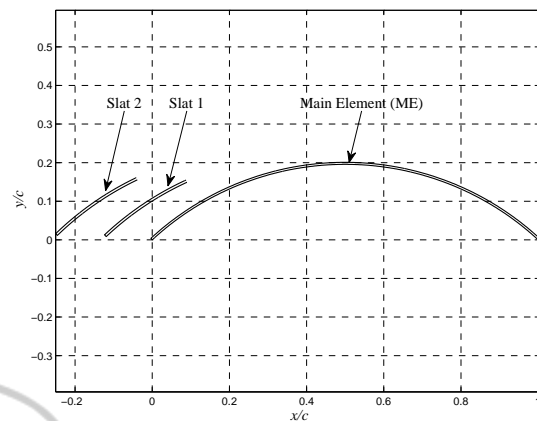


Figure 3: Cross-section of the normalized F11 trawl-door with three elements, main element (ME), slat 1 and slat 2.

### 2.2 Governing Equations

Trawl-doors are devices used in seawater, hence, we can safely assume that the flow is incompressible. We, furthermore, assume that the flow is steady, viscous and with no body forces. The Reynolds Average Navier-Stokes (RANS) equations are taken to be the governing equations with Menter's  $k-\omega$ -SST turbulence model (see for example (Tannehill et al., 1997)).

### 2.3 Computational Grid

The farfield is configured in a box-topology where the trawl-door geometry is placed in the center of the box. The main element leading edge (LE) is placed as the origin  $(x/c, y/c) = (0, 0)$ , with the farfield extending 100 main element chord lengths away from the origin. The grid is an unstructured triangular grid where the elements are clustered around the trawl-door geometry, growing in size as they move away from the origin. The maximum element size on the geometry is set to 0.1% of  $c$ . The maximum element size in domain is  $10c$ . In order to capture the viscous boundary layer well, a prismatic inflation layer is extruded from all surfaces. The inflation layer has a initial height of  $5 \times 10^{-6}c$ , growing with exponential growth ratio of 1.2 and extending 20 layers from the surface. The initial layer height is chosen so that  $y^+ < 1$ . In the wake region aft of the trawl-door, the grid is made denser by applying a density grid with an element size of 5% of  $c$ , extending  $20c$  aft of the trawl-door geometry. The density mesh is configured in an adaptive manner so that it aligns with the flow direction. An example grid is shown in Fig. 4.

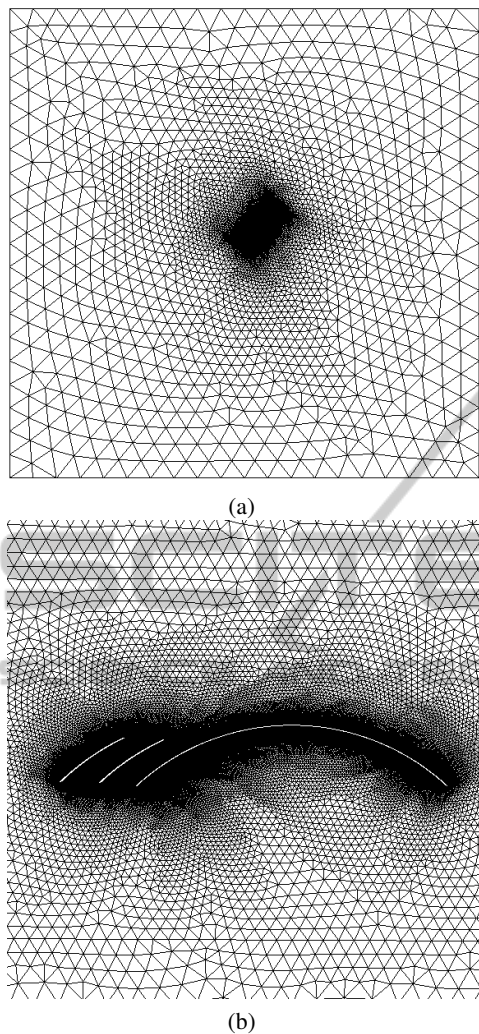


Figure 4: High-fidelity mesh for the angle of attack  $\alpha = 50$  degrees.

## 2.4 Flow Solver

Numerical fluid flow simulations are performed using the computer code ANSYS FLUENT (ANSYS, 2010). The flow solver is set to a coupled velocity-pressure-based formulation. The spatial discretization schemes are second order for all variables and the gradient information is found using the Green-Gauss node based method. Additionally, due to the difficult flow condition at high angle of attacks, the pseudo-transient option and high-order relaxation terms are used in order to get a stable converged solution (ANSYS, 2010). The iterative solution is performed with relaxation factors to prevent a numerical oscillation of the solution that can lead to a no solution or errors. The residuals, which are the sum of the  $L^2$  norm of all governing equations in each cell, are monitored

and checked for convergence. The convergence criterion for the high-fidelity model is such that a solution is considered to be converged if the residuals have dropped by six orders of magnitude, or the total number of iterations has reached 1000. Also, the lift and drag coefficients are monitored for convergence.

The working fluid used is water and the inlet boundary is a velocity-inlet with a freestream velocity  $V_\infty = 2 \text{ m/s}$ , (which is typical during trawling), split into its  $x$  and  $y$  components depending on the angle of attack  $\alpha$ . The outlet boundary is a pressure-outlet. Reynolds number is  $Re_c = 2 \times 10^{-6}$ . The inlet flow is assumed to be calm, with turbulent intensity and viscosity ratio of 0.05% and 1, respectively.

## 2.5 Grid Convergence

A sufficiently fine enough mesh is found by carrying out a grid convergence study using the NACA 0012 airfoil at  $V_\infty = 2 \text{ m/s}$ ,  $Re = 2 \times 10^6$ , and  $\alpha = 3^\circ$ . The results are shown in Fig. 5 and reveal that 197,620 grid elements are needed for convergence. The overall simulation time needed for one high-fidelity CFD simulation was around 16 minutes, executed on four Intel-i7-2600 processors in parallel (1000 solver iterations where required).

## 2.6 Model Validation

Due to a lack of available two-dimensional experimental data for trawl-door shapes, we use other types of geometries to validate the high-fidelity CFD model. The NACA 4 digit airfoils (Abbott and Von Doenhoff, 1959) have been studied extensively in the past and we consider the NACA 0012 airfoil as the validation case. The results are shown in Fig. 6. There is good agreement between the CFD model and the experimental data in terms of lift up to the stall region, and up to  $\alpha < 10^\circ$  for drag.

## 3 OPTIMIZATION WITH SPACE MAPPING

In this paper, the airfoil design is carried out in a computationally efficient manner by exploiting the space mapping (SM) methodology (Bandler et al., 2004). Space mapping replaces the direct optimization of an expensive (high-fidelity or fine) airfoil model  $f$  obtained through high-fidelity CFD simulation, by an iterative updating and re-optimization of a cheaper surrogate model  $s$ . The key component of SM is a physics-based low-fidelity (or coarse) model  $c$  that embeds certain knowledge about the system under

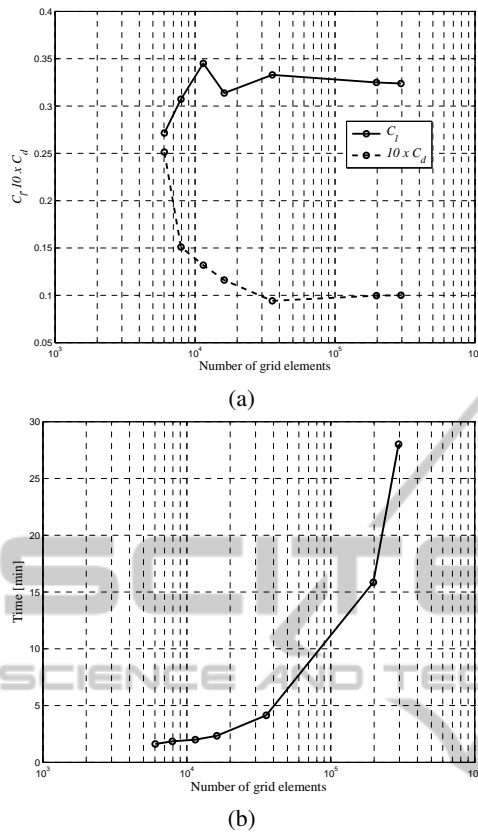


Figure 5: Grid convergence study using the NACA 0012 airfoil at  $V_\infty = 2m/s, Re = 2 \times 10^6$  and angle of attack  $\alpha = 3^\circ$ . a) Lift ( $C_l$ ) and drag ( $C_d$ ) coefficient versus number of grid elements, b) simulation time versus number of grid elements.

consideration and allows us to construct a reliable surrogate using a limited amount of high-fidelity model data. Here, the low-fidelity model is evaluated using the same CFD solver as the high-fidelity one, so that both models share the same knowledge of the airfoil performance.

### 3.1 Optimization Problem

The simulation-driven design can be generally formulated as a nonlinear minimization problem

$$\mathbf{x}^* = \arg \min_{\mathbf{x}} H(f(\mathbf{x})), \quad (1)$$

where  $\mathbf{x}$  is a vector of design parameters,  $f$  the high-fidelity model to be minimized at  $\mathbf{x}$  and  $H$  is the objective function.  $\mathbf{x}^*$  is the optimum design vector. The high-fidelity model will represent the aerodynamic forces, i.e., the lift and drag coefficients. The response will have to form

$$f(\mathbf{x}) = [C_{l,f}(\mathbf{x}), C_{d,f}(\mathbf{x})]^T, \quad (2)$$

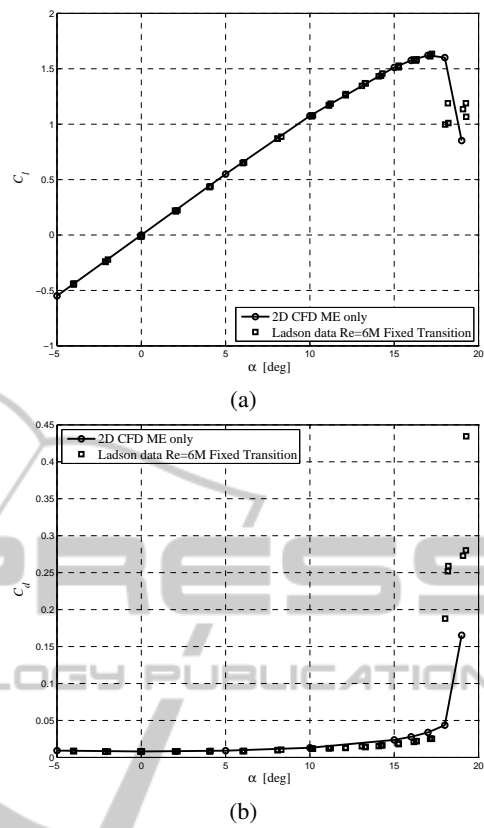


Figure 6: Results of the CFD model validation. The model is compared with experimental data (LADSON, 1988) at  $Re_c = 6 \times 10^6$ . (a) Lift curve, and (b) drag curve.

where  $C_{l,f}$  and  $C_{d,f}$  are the lift and drag coefficient, respectively, generated by the high-fidelity CFD model. We are interested in minimizing the drag for a given lift, so the objective function will take the form of

$$H(f(\mathbf{x})) = C_d, \quad (3)$$

with the design constraint written as

$$c(f(\mathbf{x})) = -C_{l,f}(\mathbf{x}) + C_{l,\min} \leq 0, \quad (4)$$

$$(5)$$

where  $C_{l,\min}$  is the minimum required lift coefficient.

### 3.2 Space Mapping Basics

Starting from an initial design  $\mathbf{x}^{(0)}$ , the generic space mapping algorithm produces a sequence  $\mathbf{x}^{(i)}, i = 0, 1, \dots$  of approximate solution to 1 as

$$\mathbf{x}^{(i+1)} = \arg \min_{\mathbf{x}} H(s^{(i)}(\mathbf{x})), \quad (6)$$

where

$$s^{(i)}(\mathbf{x}) = [C_{l,s}^{(i)}(\mathbf{x}), C_{d,s}^{(i)}(\mathbf{x})]^T, \quad (7)$$

is the surrogate model at iteration  $i$ . As previously described, the accurate high-fidelity CFD model  $f$  is accurate but computationally expensive. Using Space Mapping, the surrogate  $s$  is a composition of the low-fidelity CFD model  $c$  and a simple linear transformations to correct the low-fidelity model response (Bandler et al., 2004). The corrected response is denoted as  $s(\mathbf{x}, \mathbf{p})$  where  $\mathbf{p}$  represent a set of model parameters and at iteration  $i$  the surrogate is

$$s^{(i)}(\mathbf{x}) = s(\mathbf{x}, \mathbf{p}). \quad (8)$$

The SM parameters  $\mathbf{p}$  are determined through a parameter extraction (PE) process. In general this process is a nonlinear optimization problem where the objective is to minimize the misalignment of surrogate response at some or all previous iteration high-fidelity model data points (Bandler et al., 2004). The PE optimization problem can be defined as

$$\mathbf{p}^{(i)} = \arg \min_{\mathbf{p}} \sum_{k=0}^i w_{i,k} \|f(\mathbf{x}^{(k)}) - s(\mathbf{x}^{(k)}, \mathbf{p})\|^2, \quad (9)$$

where  $w_{i,k}$  are weight factors that control how much impact previous iterations affect the SM parameters. Popular choices are

$$w_{i,k} = 1 \quad \forall i, k, \quad (10)$$

and

$$w_{i,k} = \begin{cases} 1 & k = i \\ 0 & \text{otherwise} \end{cases}. \quad (11)$$

In the first case, all previous SM iterations influence the parameters; in the second case, the parameters depend only on the most recent SM iteration.

### 3.3 Low-fidelity CFD Model

The general underlying low-fidelity model  $c$  used for all cases is constructed in the same way as the high-fidelity model  $f$ , but with a coarser grid discretization and relaxed convergence criteria. Referring back to the grid study, carried out in Section 2.5, and inspecting Fig. 5, we select the coarse low-fidelity model. Based on time and accuracy, with respect to lift and drag, we select the grid parameters representing the fourth point from the right, giving 16,160 elements for the low-fidelity CFD model. The evaluation time of the low-fidelity model is 2.3 minutes on four Intel-i7-2600 processors in parallel. Inspecting further the lift and drag convergence plot for the low-fidelity model in Fig. 7, we note that the solution has converged after 150-200 iterations. However, the maximum number of iterations for the low-fidelity model is set to

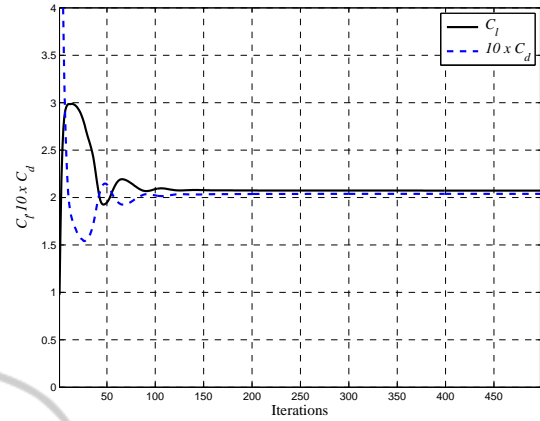


Figure 7: Lift and Drag coefficient convergence plot for low-fidelity model obtained in grid convergence study simulation for NACA 0012 at Reynolds number  $Re = 2 \times 10^6$  and angle of attack  $\alpha = 3^\circ$ .

three times that, or 700 iterations, due to the nature of problem and different geometries to be optimized. This reduces the overall simulation time to 1.6 minutes. The ratio of simulation times of the high- and low- fidelity model in this case is high/low = 16/1.6 = 10. This is based on the solver uses all 700 iterations in the low-fidelity model to obtain a solution.

### 3.4 Surrogate Model Construction

As mentioned above, the SM surrogate model  $s$  is a composition of the low-fidelity CFD model  $c$  and corrections or linear transformations where model parameters  $\mathbf{p}$  are extracted using one of the PE processes described above. Parameter extraction and surrogate optimization create a certain overhead on the whole process which can be up to 80-90 % of the computational cost. This is due to the fact that physics-based low-fidelity models are in general relatively expensive to evaluate.

To alleviate this problem, an output SM with both multiplicative and additive response correction is exploited here with the surrogate model parameters extracted analytically. We use the following formulation

$$s^{(i)}(\mathbf{x}) = \mathbf{A}^{(i)} \circ c(\mathbf{x}) + \mathbf{D}^{(i)} + \mathbf{q}^{(i)}, \quad (12)$$

or

$$s^{(i)}(\mathbf{x}) = \left[ a_l^{(i)} C_{l,c}(\mathbf{x}) + d_l^{(i)} + q_l^{(i)}, \right. \\ \left. a_d^{(i)} C_{d,c}(\mathbf{x}) + d_d^{(i)} + q_d^{(i)} \right]^T. \quad (13)$$

The parameters  $\mathbf{A}^{(i)}$  and  $\mathbf{D}^{(i)}$  are obtained by solving

$$[\mathbf{A}^{(i)}, \mathbf{D}^{(i)}] = \arg \min_{\mathbf{A}, \mathbf{D}} \sum_{k=0}^i \|f(\mathbf{x}^{(k)}) - \mathbf{A} \circ c(\mathbf{x}^{(k)}) + \mathbf{D}\|^2, \quad (14)$$

where  $w_{i,k} = 1$ , i.e., all previous iteration points are used to improve globally the response of the low-fidelity model. The additive term  $q^{(i)}$  is defined such it ensures a perfect match between the surrogate and the high-fidelity model at design  $\mathbf{x}^{(i)}$ , namely  $f(\mathbf{x}^{(i)}) = s(\mathbf{x}^{(i)})$  or a zero-order consistency (Alexandrov and Lewis, 2001). We can write the additive term as

$$q^{(i)} = f(\mathbf{x}^{(i)}) - [\mathbf{A}^{(i)} \circ c(\mathbf{x}^{(i)}) + \mathbf{D}^{(i)}]. \quad (15)$$

Since an analytical solution exists for  $\mathbf{A}^{(i)}, \mathbf{D}^{(i)}$  and  $\mathbf{q}^{(i)}$  there is no need for non-linear optimization solving Eq. 9 to obtain the parameters. We can obtain  $\mathbf{A}^{(i)}$  and  $\mathbf{D}^{(i)}$  by solving

$$\begin{bmatrix} a_l^{(i)} \\ d_l^{(i)} \end{bmatrix} = (\mathbf{C}_l^T \mathbf{C}_l)^{-1} \mathbf{C}_l^T \mathbf{F}_l, \quad (16)$$

$$\begin{bmatrix} a_d^{(i)} \\ d_d^{(i)} \end{bmatrix} = (\mathbf{C}_d^T \mathbf{C}_d)^{-1} \mathbf{C}_d^T \mathbf{F}_d, \quad (17)$$

where

$$\mathbf{C}_l = \begin{bmatrix} C_{l,c}(\mathbf{x}^{(0)}) & C_{l,c}(\mathbf{x}^{(1)}) & \dots & C_{l,c}(\mathbf{x}^{(i)}) \\ 1 & 1 & \dots & 1 \end{bmatrix}^T, \quad (18)$$

$$\mathbf{F}_l = \begin{bmatrix} C_{l,f}(\mathbf{x}^{(0)}) & C_{l,f}(\mathbf{x}^{(1)}) & \dots & C_{l,f}(\mathbf{x}^{(i)}) \\ 1 & 1 & \dots & 1 \end{bmatrix}^T, \quad (19)$$

$$\mathbf{C}_d = \begin{bmatrix} C_{d,c}(\mathbf{x}^{(0)}) & C_{d,c}(\mathbf{x}^{(1)}) & \dots & C_{d,c}(\mathbf{x}^{(i)}) \\ 1 & 1 & \dots & 1 \end{bmatrix}^T, \quad (20)$$

$$\mathbf{F}_d = \begin{bmatrix} C_{d,f}(\mathbf{x}^{(0)}) & C_{d,f}(\mathbf{x}^{(1)}) & \dots & C_{d,f}(\mathbf{x}^{(i)}) \\ 1 & 1 & \dots & 1 \end{bmatrix}^T, \quad (21)$$

which are the least-square optimal solutions to the linear regression problems

$$\mathbf{C}_l a_l^{(i)} + d_l^{(i)} = \mathbf{F}_l, \quad (22)$$

$$\mathbf{C}_d a_d^{(i)} + d_d^{(i)} = \mathbf{F}_d. \quad (23)$$

Note that  $\mathbf{C}_l^T \mathbf{C}_l$  and  $\mathbf{C}_d^T \mathbf{C}_d$  are non-singular for  $i > 1$  and assuming that  $\mathbf{x}^{(k)} \neq \mathbf{x}^{(i)}$  for  $k \neq i$ . For  $i = 1$  only the multiplicative SM correction with  $\mathbf{A}^{(i)}$  is used.

### 3.5 Optimization Algorithm

Here we formulate the optimization algorithm exploiting the SM based surrogate and a trust-region convergence safeguard (Forrester and Keane, 2009). The trust-region parameter  $\lambda$  is updated after each iteration. This algorithm will be used in applications presented in this thesis.

1. Set  $i = 0$ ; Select  $\lambda$ , the trust region radius; Evaluate the high-fidelity model at the initial solution,  $f(\mathbf{x}^{(0)})$ ;
2. Using data from the low-fidelity model  $c$ , and  $f$  at  $\mathbf{x}^{(k)}, k = 0, 1, \dots, i$ , setup the SM surrogate  $s^{(i)}$ ; Perform PE;
3. Optimize  $s^{(i)}$  to obtain  $\mathbf{x}^{(i+1)}$ ;
4. Evaluate  $f(\mathbf{x}^{(i+1)})$ ;
5. If  $H(f(\mathbf{x}^{(i+1)})) < H(f(\mathbf{x}^{(i)}))$ , accept  $\mathbf{x}^{(i+1)}$ ; Otherwise set  $\mathbf{x}^{(i+1)} = \mathbf{x}^{(i)}$ ;
6. Update  $\lambda$ ;
7. Set  $i = i + 1$ ;
8. If the termination condition is not satisfied, go to 2, else proceed;
9. End; Return  $\mathbf{x}^{(i)}$  as the optimum solution.

The termination condition is set to  $\|\mathbf{x}^{(i)} - \mathbf{x}^{(i-1)}\| < 10^{-3}$ .

## 4 PERFORMANCE ANALYSIS

In this section, we present the results of the CFD analysis of the two-dimensional cut of the F11 trawl-door, shown in Fig. 3. The CFD model, presented in Section 2, is evaluated at number of different angle of attacks or from  $\alpha = -5^\circ$  to  $\alpha = 60^\circ$  with 5 degree increments at a free-stream velocity  $V_\infty = 2 \text{ m/s}$ , and Reynolds number  $Re_c = 2 \times 10^6$ . Three different configurations were studied: the main element only, the main element with one slat, and the main element with two slats (the F11 trawl-door design). Figure 8 shows the lift and drag curves.

Inspecting Fig. 8 reveals that the flow remains attached for relatively low angles of attack when considering the main element only, and stall occurs close to  $\alpha = 10^\circ$ . For the main element with one slat, the stall occurs at  $\alpha = 20^\circ$  and for the F11 design (the main element with two slats) the stall occurs at  $\alpha = 25^\circ$ . Adding the slats therefore to improves the performance by delaying the stall, as well as increasing the  $C_{l,\max}$ . This effect is expected as it is well known for multi-element high-lift devices on aircraft.

We can split Fig. 8(b) into three regions, first where the stall has not occurred where  $\alpha < 20^\circ$ , and after stalling  $20^\circ < \alpha < 35^\circ$  and  $\alpha > 35^\circ$ . As seen in part  $\alpha < 20^\circ$ , prior to stall, the drag increases as more slats are added to the assembly simply because of more area that the flow needs to bypass. As the angle of attack is increased beyond stall, the drag rises due to a massive flow separation as can be seen in Fig. 9. Effectiveness of slats is evident here, whereas by adding slats the flow remains attached longer reducing separation and drag. In the last region,  $\alpha > 35^\circ$ , the flow simply needs to pass through more area as more slats are added, increasing the drag further.

It should be noted that the flow is highly unsteady, especially for large angles of attack, i.e., higher than 20 degrees. Therefore, the steady-state model does not give an accurate description of the flow and only provides an estimate of the averaged characteristics. Any flow analysis or design optimization at high angles of attack should be performed using an unsteady analysis. However, a steady-state model gives a reasonable estimate at moderate angles of attack.

## 5 DESIGN OPTIMIZATION

We proceed with a low angle of attack steady-state analysis working only in the range where separation is limited, thus, avoiding strong unsteady effects. The objective is to optimize the location of the one slat design to match or exceed the performance of the F11 trawl-door. We consider a drag minimization formulation solved using both direct optimization using the pattern-search technique (Kolda et al., 2003) and the space mapping (SM) methodology presented in Section 3.

### 5.1 Problem Formulation

To simplify the geometry, the slat furthest upstream of the F11 design is removed and we consider only the remaining geometry for optimization. The design variables considered are the location of the slat  $(x_{S1}/c, y_{S1}/c)$ , the slat orientation  $\theta_{S1}$ , and the angle of attack  $\alpha$  of the flow. This is shown in Fig. 10. The design vector is written as  $\mathbf{x} = [x_{S1}/c, y_{S1}/c, \theta_{S1}, \alpha]^T$ . The free-stream velocity is fixed at  $V_\infty = 2 \text{ m/s}$  and the Reynolds number is  $Re_c = 2 \times 10^6$ .

The objective is to minimize the drag coefficient  $C_{d,f}$  subject to a constraint on the lift coefficient  $C_{l,f} \geq C_{l,\min} = 1.5$ . Additional constraints include a geometry validity check where the design is checked at every iteration such that the optimizer rejects designs if the slat and the main element cross, or vio-

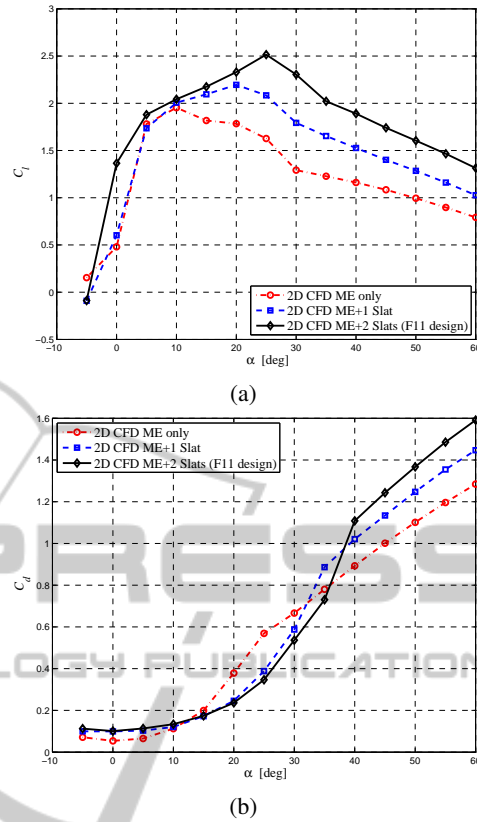


Figure 8: Lift and drag curves at  $V_\infty = 2 \text{ m/s}$ ,  $Re_c = 2 \times 10^6$ . Computational results are shown with dotted dash line (.-), dashed line (- -) and solid line (-) for Main Element only (ME), ME + 1 slat and ME + 2 (the F11 trawl-door design) respectively. (a) lift coefficient, (b) drag coefficient.

late a minimum gap,  $Gap \geq Gap_{\min}$ , or a maximum overlap,  $Overlap \leq Overlap_{\max}$ . The minimum gap between elements is defined as the minimum distance from any point on the main element to any point on the slat. Maximum overlap is defined as the distance  $x/c$  which the trailing edge of the slat overlaps the leading edge of the main element.

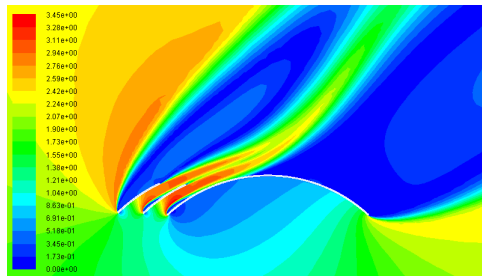
The nonlinear minimization problem is formulated as

$$\mathbf{x}^* = \arg \min_{\mathbf{x}} C_d, \quad (24)$$

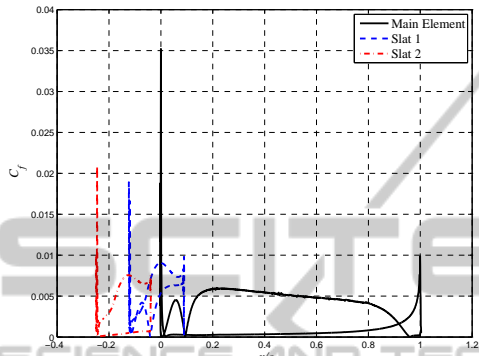
subject to

$$\begin{aligned} C_{l,f} &\geq C_{l,\min} = 1.5, \\ Gap &\geq Gap_{\min} = 0.05, \\ Overlap &\leq Overlap_{\max} = 0.1, \end{aligned} \quad (25)$$

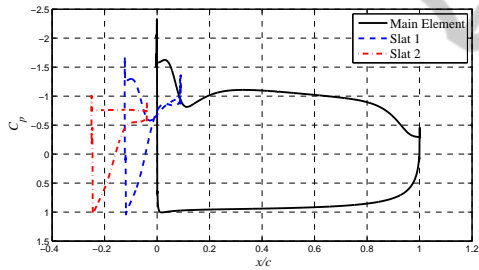
with the following design variable bounds



(a)



(b)



(c)

Figure 9: F11 trawl-door characteristics at  $V_\infty = 2m/s, Re_c = 2 \times 10^6$ , angle of attack  $\alpha = 40^\circ$ . (a) Velocity contours, (b) Skin friction coefficient ( $C_f$ ), (c) Pressure coefficient ( $C_p$ ).

$$\begin{aligned} -0.3 \leq x_{S1}/c \leq 0.2, \\ -0.3 \leq y_{S1}/c \leq 0.2, \\ 20 \leq \theta_{S1} \leq 50, \\ 2 \leq \alpha \leq 8. \end{aligned} \quad (26)$$

## 5.2 Results

The numerical results are given in Table 1. Results using the proposed SM method are compared to the initial design of the modified F11 geometry design (two elements, main element and one slat), and the

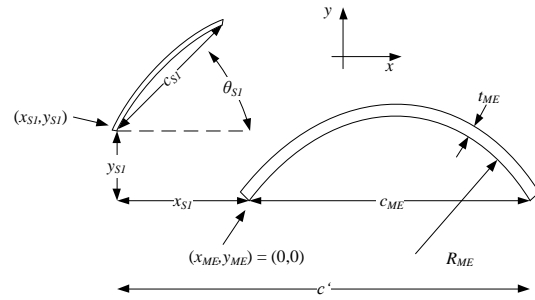


Figure 10: Shift  $(x_{S1}, y_{S1})$  relative to  $(0,0)$  and orientation  $\theta_{S1}$  of one slat. The second slat is omitted for simplicity. The chord length  $c$  of each element is defined from its leading edge to trailing edge and  $c'$  is the extended chord length for the assembly. Thickness  $t_{ME}$  and radius  $R_{ME}$  for the ME are shown but omitted for slat.

direct optimization of that design. Figure 11 shows the initial and optimized designs. Figure 12 shows the flow field, as well as the skin friction and pressure distributions.

Similar results are obtained by the direct approach and the SM approach. The slat is moved down and forward, and tilted clockwise. The angle of attack is reduced to between 2 to 3 degrees. The optimized trawl-door design has approximately 90% less drag for a lift coefficient of approximately 1.5 (the SM approach slightly violates the lift constraint by less than 5%). The proposed method requires less than 31 high-fidelity model evaluations, 250 surrogate and 5 high-fidelity which is considerably lower than if direct optimization is applied which required 180 high-fidelity model evaluations.

A comparison of the optimized SM design with the F11 design is given in Table 2 at  $C_l = 1.4382$ . At this  $C_l$ , the F11 design is operating at 56 degrees (referring to Fig. 8), with a drag coefficient of about 96% lower than the optimized design. The drag reduction comes about due to a reduction in the angle of attack and associated attached flow on the upper surface as can be seen from Fig. 12. The F11 design has a lift-to-drag ratio around 1, whereas the optimized design lift-to-drag-ratio is around 23.

## 6 CONCLUSIONS

A robust and efficient design optimization methodology of fishing gear trawl-doors using high-fidelity CFD models has been presented. The steady-state two-dimensional high-fidelity CFD model captures the essence of the complex flow physics of the trawl-door flow. The computational cost of the design process is reduced significantly by using a surrogate-based optimization technique with variable-resolution

Table 1: Numerical results initial, direct and surrogate based optimization using space mapping. The ratio of the high-fidelity model evaluation time to the low-fidelity is 10. The ratio is the SM optimized design over the initial design.

Variable	Initial	Direct	SM	Ratio
$x/c$	-0.1192	-0.2515	-0.2107	-
$y/c$	0.0085	-0.0298	-0.0100	-
$\theta$ [deg]	33.9	22.3648	24.0113	-
$\alpha$ [deg]	30.0	2.8058	2.0000	-
$C_l$	1.7925	1.5634	1.4382	0.8
$C_d$	0.5875	0.0613	0.0614	0.1
$C_l/C_d$	3.0511	25.5041	23.4235	7.7
$N_c$	-	300	250	-
$N_f$	-	150	6	-
Total Cost	-	180	< 31	-

Table 2: Space mapping optimum design compared to the F11 trawl-door design at lift coefficient  $C_l = 1.4382$ . The ratio is the SM optimized design over the F11 design.

Variable	F11 design	SM	Ratio
$\alpha$ [deg]	55.9	2.0000	-
$C_d$	1.5044	0.0614	0.04
$C_l/C_d$	0.9560	23.4235	24.5

CFD models.

The results of a performance analysis show that the current trawl-door designs are poorly designed in terms of efficiency. The flow is massively separated at the high operation angle of attack (between 30 to 50 degrees), resulting in large vortices being shed and yielding a highly unsteady response. However, the leading-edge slats alleviate the lift loss a bit by extending the stall angle of attack up to 25 to 30 degrees.

A design optimization of the slat position shows that the operation angle of attack can be lowered sig-

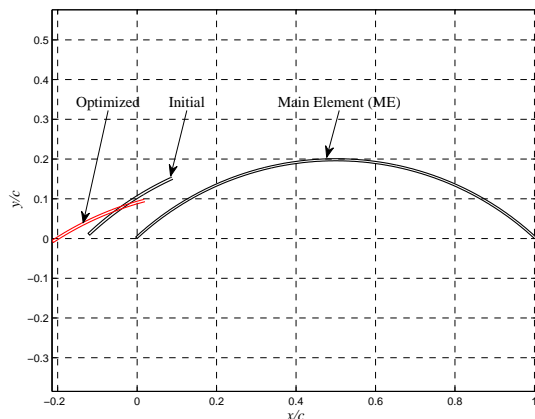
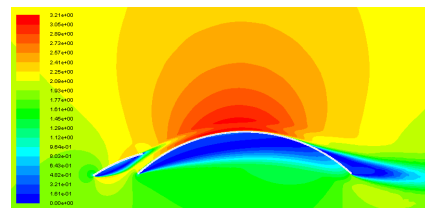
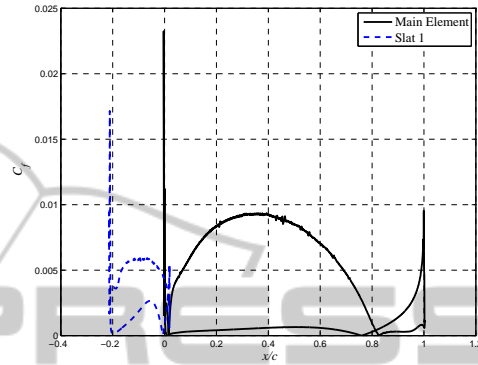


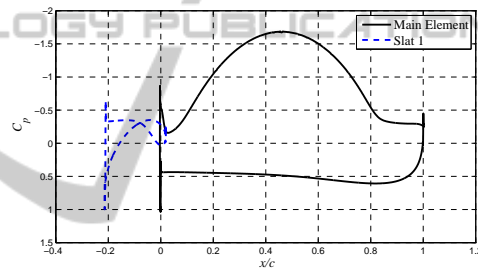
Figure 11: Optimum design geometry obtained using space mapping with the initial design shown as well.



(a)



(b)



(c)

Figure 12: Space Mapping optimization results  $V_\infty = 2m/s, Re_c = 2 \times 10^6$ . Optimized design characteristics at angle of attack  $\alpha = 2^\circ$ . a) Velocity contour, b) Skin friction coefficient ( $C_f$ ), c) Pressure coefficient ( $C_p$ ).

nificantly (to almost zero) and still retain the required lift. As a result, the flow remains attached and the drag is reduced dramatically, yield a large improvement in efficiency, which could translate to lowered fuel consumption of the fishing vessel. These results give rise to further study of trawl-door shapes, as the potential benefit is very important.

## ACKNOWLEDGEMENTS

This work was funded by RANNIS, The Icelandic Research Fund for Graduate Students, grant ID: 110395-0061

## REFERENCES

- Abbott, I. and Von Doenhoff, A. (1959). *Theory of wing sections: including a summary of airfoil data*. Dover Pubns.
- Alexandrov, N. and Lewis, R. (2001). An overview of first-order model management for engineering optimization. *Optimization and Engineering*, 2(4):413–430.
- ANSYS (2010). *ANSYS FLUENT Theory Guide*. ANSYS, Southpointe 275 Thecnology Drive Canonburg PA 15317, release 13.0 edition.
- Bandler, J., Cheng, Q., Dakrouy, S., Mohamed, A., Bakr, M., Madsen, K., and Sondergaard, J. (2004). Space mapping: the state of the art. *Microwave Theory and Techniques, IEEE Transactions on*, 52(1):337–361.
- Forrester, A. and Keane, A. (2009). Recent advances in surrogate-based optimization. *Progress in Aerospace Sciences*, 45(1-3):50–79.
- Garner, J. (1967). *Botnvarpan og bunadur hennar*. Fiskifélag Islands.
- Haraldsson, H. O., Brynjolfsson, S., and Jnsson, V. K. (1996). Reiknileg hermun iustreymis umhverfis toghlera. *Vlabrg*, 17.rg.:31–35.
- Kolda, T., Lewis, R., and Torczon, V. (2003). Optimization by direct search: New perspectives on some classical and modern methods. *SIAM review*, pages 385–482.
- Koziel, S. and Leifsson, L. (2012). Knowledge-based airfoil shape optimization using space mapping. In *22nd AIAA Applied Aerodynamics Conference*.
- LADSON, C. (1988). Effects of independent variation of mach and reynolds numbers on the low-speed aerodynamic characteristics of the naca 0012 airfoil section.
- Tannehill, J., Anderson, D., and Pletcher, R. (1997). *Computational fluid mechanics and heat transfer*. Taylor & Francis Group.